Geophysical Journal International

Noise-based Ballistic Wave Passive Seismic Monitoring - Part 2: Surface Waves

Journal:	*Geophysical Journal International*
Manuscript ID	GJI-19-0346
Manuscript Type:	Research Paper
Date Submitted by the Author:	17-Apr-2019
Complete List of Authors:	Mordret, Aurélien; Massachusetts Institute of Technology, Department of Earth, Atmospheric and Planetary Sciences Courbis, Roméo; Univ. Grenoble Alpes, ISTerre Brenguier, Florent ; Univ. Grenoble Alpes, ISTerre Chmiel, Malgorzata; Univ. Grenoble Alpes, ISTerre Garambois, Stéphane; Institut des Sciences de la Terre, OMIV Mao, Shujuan; Massachusetts Institute of Technology, Department of Earth, Atmospheric and Planetary Sciences Boué, Pierre; Université Joseph Fourier, ISTerre Campman, Xander; Shell International Exploration and Production B.V., ; MIT, ERL Lecocq, Thomas; Royal Observatory of Belgium, Seismology Van der Veen, Wim ; Nederlandse Aardolie Maatschappij BV Hollis, Daniel; Sisprobe
Keywords:	Seismic tomography < SEISMOLOGY, Seismic interferometry < SEISMOLOGY, Wave scattering and diffraction < SEISMOLOGY, Wave propagation < SEISMOLOGY, Surface waves and free oscillations < SEISMOLOGY

submitted to *Geophys. J. Int.*

Noise-based Ballistic Wave Passive Seismic Monitoring – Part 2: Surface Waves

Aurélien Mordret[1⋆], Roméo Courbis[2−3], Florent Brenguier[2], Małgorzata Chmiel[2−3], Stéphane Garambois[2], Shujuan Mao[1], Pierre Boué[2], Xander Campman[4], Thomas Lecocq[5], Wim Van der Veen[6] and Dan Hollis[3]

[1]*Department of Earth, Atmospheric and Planetary Sciences, Massachusetts Institute of Technology (MIT), Cambridge, Massachusetts, USA*

[2]*Université Grenoble Alpes, Univ. Savoie Mont Blanc, CNRS, IRD, IFSTTAR, ISTerre, UMR 5275, 38000 Grenoble, France*

[3]*Sisprobe, Meylan, 38240, France*

[4]*Shell Global Solutions International BV, Amsterdam, the Netherlands*

[5]*Royal Observatory of Belgium - Seismology, Avenue Circulaire, 3, BE-1180 Brussels, Belgium*

[6]*Nederlandse Aardolie Maatschappij.*

17 April 2019

SUMMARY

We develop a new method to monitor and locate seismic velocity changes in the subsurface using seismic noise interferometry. We use the ballistic Rayleigh waves computed from 30 days records on a dense nodal array located above the Groningen gas field (the Netherlands). We infer the daily relative phase velocity dispersion changes as a function of frequency and propagation distance with a cross-wavelet transform processing. Assuming a one-dimensional velocity change within the medium, the induced ballistic Rayleigh wave phase shift exhibits a linear trend as a function of the propagation distance. Measuring this trend for the fundamental mode and the first overtone of the Rayleigh waves for frequencies between 0.5 and 1 Hz enables us to invert for shear-wave daily velocity changes in the first 1.5 km of the subsurface.

Most of the changes are observed in a carbonate layer below 800 m depth. Combined with P-wave velocity changes observations from a companion study (Brenguier et al. 2019), we interpret the changes as caused by slight water saturation variations induced by deep fluid flows.

Key words: Seismic tomography; Seismic interferometry; Wave scattering and diffraction; Wave propagation; Surface waves and free oscillations

1 INTRODUCTION

Ambient seismic noise interferometry (e.g., Shapiro & Campillo 2004; Wapenaar et al. 2010) via Coda Wave Interferometry (CWI, e.g., Snieder et al. 2002; Sens-Schönfelder & Wegler 2006; Brenguier et al. 2008b) has become the most efficient way to probe continuous temporal changes of the elastic properties of the crust. It has successfully been applied to volcano monitoring during pre- and co-eruptive stages (Brenguier et al. 2008b; Mordret et al. 2010; Yukutake et al. 2016) or inter-eruptive periods (e.g., Sens-Schönfelder & Wegler 2006; Rivet et al. 2014; Donaldson et al. 2017). It has also been used to monitor the response of the crust to large earthquakes (e.g., Wegler & Sens-Schönfelder 2007; Brenguier et al. 2008a; Minato et al. 2012; Brenguier et al. 2014) or slow-slip events (Rivet et al. 2011). More recently, it has contributed to the fast emergence of environmental seismology applications (Mainsant et al. 2012; Gassenmeier et al. 2014; Larose et al. 2015; Mordret et al. 2016; Lecocq et al. 2017; Clements & Denolle 2018; Mao et al. 2018; Fores et al. 2018) and passive seismic monitoring of civil engineering structures (Nakata & Snieder 2013; Salvermoser et al. 2015; Planès et al. 2015; Mordret et al. 2017).

Although very robust to detect small changes in a medium (Froment et al. 2010; Weaver et al. 2011; Colombi et al. 2014), CWI lacks spatial resolution due to the inherent nature of coda waves. Statistical approaches can lead to the probability of a local change in a medium knowing the perturbation in the coda of a seismogram (Pacheco & Snieder 2005; Obermann et al. 2013) but the sensitivity kernels derived in these studies are smooth, dependant on the modal distribution of the

⋆ Corresponding author, mordret@mit.edu

waves forming the coda and on the statistical scattering properties of the medium which hamper a precise localization of the changes and proper estimate of their real amplitude.

In this work and a companion paper (Brenguier et al. 2019) we propose to overcome these limitations by using a new complementary method for monitoring seismic velocity variations based on ballistic waves reconstructed from noise correlations. The first paper (Brenguier et al. 2019) deals with body waves while this paper focuses on surface waves application. Using ballistic waves means that, contrarily to coda-waves, we have accurate models for their propagation and therefore we can project the observed temporal perturbations of seismic velocities to specific regions at depth (Voisin et al. 2016, 2017). However, the clear limitation of using direct, ballistic waves is their strong sensitivity to noise source temporal variations (Colombi et al. 2014) and the fact that they exhibit smaller time-shift than coda waves, for the same perturbation. We use advanced frequency–time analysis and a dense seismic network coupled with offset and azimuthal averaging to mitigate these issues, but one still needs to carefully analyse the stability of noise sources for such type of analysis.

Surface waves are the most easily retrieved phases in ambient noise correlations (Shapiro & Campillo 2004) because seismic noise sources are most often located at the surface and mainly generate surface waves. However, certainly because of the aforementioned drawbacks, only few attempts have been made to use direct surface waves from noise correlations to monitor the subsurface (Durand et al. 2011; Ridder et al. 2014; Mordret et al. 2014b; Toyokuni et al. 2018). In this paper we describe the basics of passive ballistic surface wave monitoring using dense arrays. We are able to measure temporal changes of apparent velocities from both fundamental mode and first overtone Rayleigh waves, which allows us to discriminate between changes localized in the shallower part or the deeper part of the subsurface, in good agreement with the P-wave monitoring results (Brenguier et al. 2019).

2 DATA

We use a network of 417 short period seismic stations deployed in the Groningen area of the Netherlands, above the Groningen gas field (Fig. 1). The array was deployed for 30 days in 2017

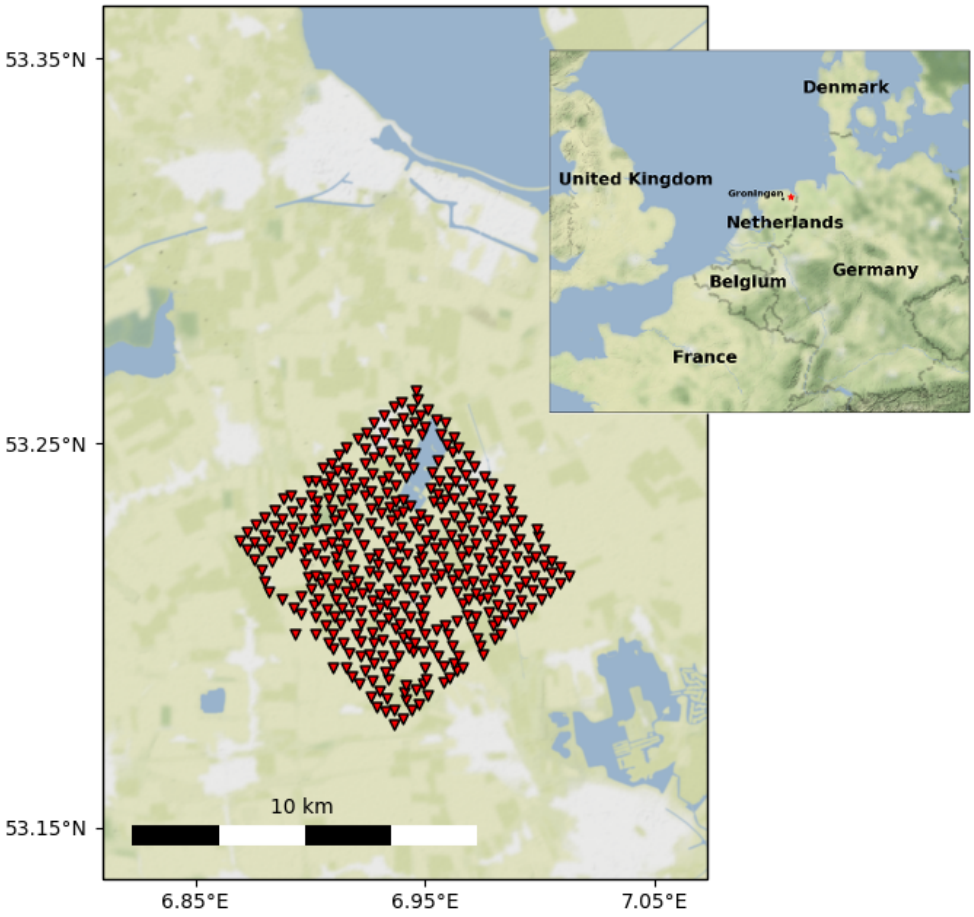

Figure 1. Map of the array of 417 sensors used in this study.

from February 11 (day 42) to March 12 (day 71) and laid out as a regular square grid with an aperture of about 8 km and a nominal inter-station distance of 300 m. The original purpose of the array was to perform high-resolution ambient seismic noise tomography to characterize the near surface for seismic hazard assessment and ground motion prediction (Chmiel et al. 2019). The gas reservoir is located at about 3 km depth in the Permian sandstones of the Rotliegend Group, it is 250 m thick and covers a 2000 km^2 area. It is sealed by a Zechstein salt layer up to 1 km thick. Above the salt layer lays a $\sim$1 km thick Cretaceous Chalk formation capped with a 800 m thick Tertiary and Quaternary sediment cover, up to the surface (van Thienen-Visser & Breunese 2015). Bourne et al. (2018) show that the gas production in this field led to a 15 MPa average reservoir pore-pressure depletion since 1995 which is associated with seismicity rates exponentially increasing with time.

We follow Chmiel et al. (2019)'s procedure for the correlation computation. We average the

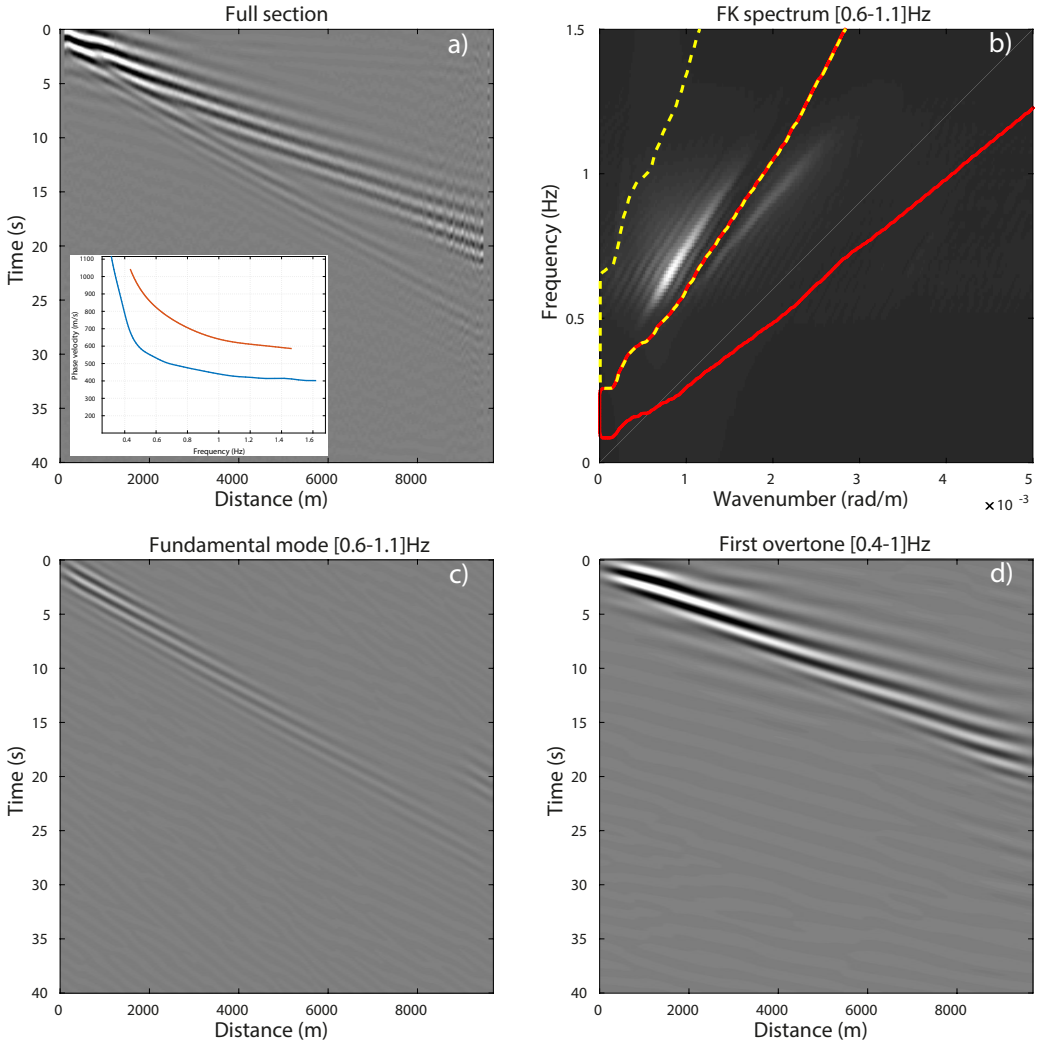

Figure 2. a) Full seismic section filtered between [0.6–1.2] Hz. The inset shows the phase velocity dispersion curves of the fundamental mode (blue) and the first overtone (red). b) FK diagram of the seismic section. The FK filter windows to extract the fundamental mode and the first overtone are shown in red and yellow, respectively. c) The FK-filtered fundamental mode band-pass filtered between [0.6–1.1]Hz. d) The FK-filtered first overtone band-pass filtered between [0.4–1.0]Hz.

causal and acausal sides of the correlations, then the symmetrized correlations are further stacked in 50 m inter-station distance bins (Boué et al. 2013; Mordret et al. 2014a; Nakata et al. 2015) to enhance the signal to noise ratio, to mitigate the azimuthal variations of noise sources and to help to converge closer to the true Green's function. This procedure effectively approximates the propagating medium as a 1-dimensional medium.

Finally, we construct a 30-days average seismic section which is used as the reference section and 21 ten-days moving average sections which are used as daily section for the monitoring. The

resulting reference virtual seismic section, filtered between [0.6–1.2] Hz, is shown in Figure 2a). We can see the faster, higher amplitude and lower frequency first overtone travelling with a group velocity of about 450 m/s and the slower and less energetic fundamental mode travelling at a speed around 330 m/s. The FK spectrum of the section is shown in Figure 2b) and is used to pick the phase velocity dispersion curves of the two modes (Fig. 2a)). In the following, we perform the monitoring measurements on each mode separately. To do so, we apply two FK-filters to each of the 22 sections (the reference and the 21 daily ones) as described in Figure 2b-c-d). The FK-filtered sections are further windowed between travel-times corresponding to [250–380] m/s and [400–1000] m/s for the fundamental mode and the first overtone, respectively. We tested the effect of the FK-filters on the final velocity variation results: not using them slightly increases the uncertainties but does not change the overall results and interpretations.

3 METHODS

3.1 Phase-shift measurement with Cross-Wavelet transform

Measuring the travel-time shift induced by a localized seismic velocity perturbation on a dispersive surface-wave requires a frequency–time representation where one is able to estimate the instantaneous phase of a seismogram in the frequency–time domain (Corciulo et al. 2012). Continuous wavelet transform (CWT) has been extensively used in Earth Science for more than two decades to analyse the frequency–time behaviour of geophysical transient signals (e.g., Kumar & Foufoula-Georgiou 1994; Pyrak-Nolte & Nolte 1995; Labat 2005) and has originally been developed to analyse active seismic traces in seismic exploration (Morlet et al. 1982b,a). This section describes the use of wavelet-transform for ballistic surface wave monitoring. A similar approach can be used for CWI applications and is the subject of a subsequent paper (Mao et al. 2019).

The CWT of a signal $s(t)$ is defined as the correlation or inner product of $s(t)$ with a particular set of functions $h_{a,b}(t)$ such as

$$\mathbf{WT}[s(t)](a,b) = \int_{-\infty}^{\infty} s(t) h^*_{a,b}(t) dt \,, \tag{1}$$

where

$$h_{a,b}(t) = \frac{h[(t-b)/a]}{\sqrt{|a|}}\,. \tag{2}$$

In these expressions, $a, b \in \mathbb{R}$, with $a \neq 0$. The $*$ symbol denotes the complex conjugate. The elements of the wavelet basis $h_{a,b}(t)$ are created by dilating and translating the mother wavelet $h(t)$ by the dilation parameters a (called scale and equivalent for frequency) and the translation parameters b. The pre-factor $\sqrt{|a|}$ ensures norm-squared normalisation. Practically, we used the CWT function from the MATLAB2018a Wavelet Toolbox to build our algorithm.

In the following analysis, we use the complex analytic Morlet wavelet (Morlet et al. 1982b,a; Teolis & Benedetto 1998) composed of a harmonic function windowed by a Gaussian filter. In the Fourier domain the Morlet wavelet is defined as:

$$\Psi(a\omega) = \pi^{-1/4} e^{-(a\omega-\omega_0)^2/2} H(a\omega)\,, \tag{3}$$

where H is the Heaviside step function, a is the scale and ω_0 the central frequency. Here, we use $\omega_0 = 6$ Hz as default value.

The resulting Morlet CWT is a 2D complex function which has both amplitude and phase information and has an optimum resolution both in time and frequency with the smallest possible Heisenberg uncertainty. It can be shown that the maximum of the CWT amplitude along the scale direction defines the group velocity dispersion curves of the transformed time-series (Pyrak-Nolte & Nolte 1995).

To compare two dispersive time-series by estimating their common power and phase relation, we use the cross-wavelet transform (Grinsted et al. 2004) which can be seen as a frequency–time cross-correlation. Let $r(t)$ be a reference seismic trace and $c(t)$ the current seismic trace we want to compare with $r(t)$. The cross-wavelet transform of r and c is

$$\mathbf{XWT}[r(t), c(t)](a,b) = \mathbf{WT}[r(t)](a,b)\mathbf{WT}^*[c(t)](a,b) = |A|e^{i\Delta\phi}\,, \tag{4}$$

where $|A|$ is the amplitude power of the cross-wavelet transform and its phase is given by the phase difference between $\mathbf{WT}[c(t)]$ and $\mathbf{WT}[r(t)]$ such as $\Delta\phi = arg\left(\mathbf{WT}[r(t)]\right) - arg\left(\mathbf{WT}[c(t)]\right)$.

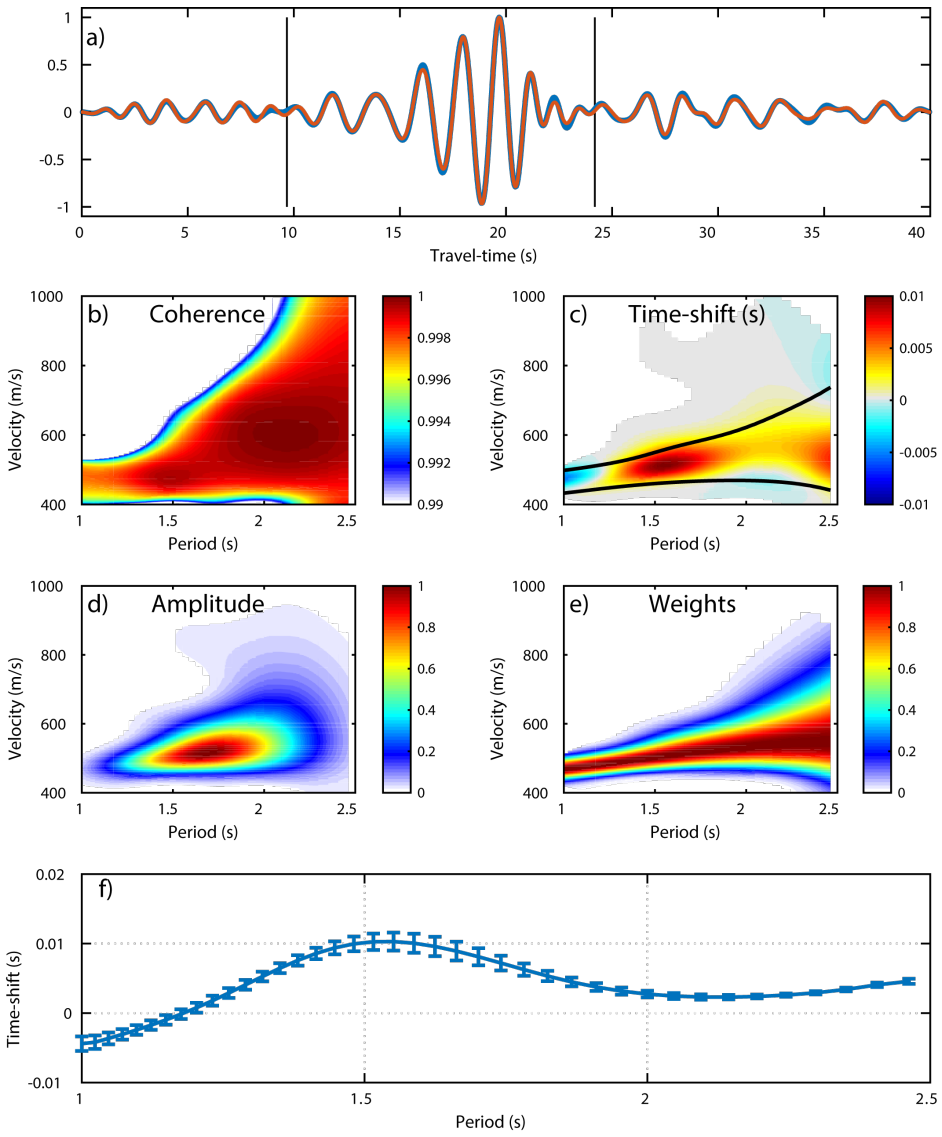

Figure 3. a) Reference (blue) and current (orange) binned correlations at 9 km distance, FK-filtered around the first overtone. The vertical black lines show the analysis window. b) Wavelet Coherence between the traces in a). c) The time-shift between the two traces multiplied by the weight function shown in e). The black contour shows where the weights are larger than 0.1. d) The normalised amplitude power of the cross-wavelet transform: $|A|$. e) The weight function. f) The weighted-average frequency-dependent time-shift, the errorbars show one standard deviation of the average.

The amplitude power of the cross-wavelet transform shows where both time-series have common high amplitudes (Fig. 3d). An other useful measure of the resemblance between the two waveform in the frequency–time domain can be defined by the wavelet coherence (Fig. 3b):

$$\mathbf{WCoh}[r(t),c(t)](a,b) = \frac{|\mathcal{S}\left\{a^{-1}|\mathbf{XWT}[r(t),c(t)](a,b)|^2\right\}|^2}{\mathcal{S}\left\{a^{-1}|\mathbf{WT}[r(t)](a,b)|^2\right\}\mathcal{S}\left\{a^{-1}|\mathbf{WT}[c(t)](a,b)|^2\right\}}\,, \tag{5}$$

where $\mathcal{S}\{\cdot\}$ is a 2D smoothing operator over the scales a and delays b. Here, we used a Gaussian smoothing window in the delays direction and a moving average (boxcar window) in the scales direction. The smoothing is necessary to avoid having a coherence of one for every samples. The wavelet coherence can be seen as a local correlation coefficient in the frequency–time domain and is bounded between [0 1]. Finally, the time-shift Δt in the frequency–time domain (Fig. 3c) between the two waveforms can be computed by

$$\Delta t(a,b) \equiv \Delta t(f,U) = \frac{\Delta\phi}{2\pi f}\,, \tag{6}$$

where f is the frequency and U the group velocity obtained by $U = D/t$, with D the distance between the source and the receiver. However, the time-shift can only be reliably estimated where the amplitudes of both reference and current traces are largely above the noise level, i.e., where $|A|$ is large enough. Following Fichtner et al. (2008), we design a weight function (Fig. 3e) that allows us to accurately extract the time-shift between the two waveforms as a function of the frequency:

$$\mathcal{W}(f,U) = (log(1+|A|)/\max_f log(1+|A|))^2 \qquad \text{if } WCoh > 0.95 \;\&\; |A|/\max_{f,U}|A| > 0.01, \tag{7}$$

$$\mathcal{W}(f,U) = 0 \qquad \text{otherwise.} \tag{8}$$

We finally obtain the frequency-dependant time-shift $\delta t(f)$ between the two waveforms by computing the weighted average of $\Delta t(f,U)$ by $\mathcal{W}(f,U)$ along the group velocity axis. We repeat this operation for every distance bins, every days and for both FK-filtered fundamental and first overtone.

3.2 Relative phase velocity change estimation

From the time-shifts measured at each frequency and each distance along the virtual seismic section, we can estimate the frequency-dependant relative phase velocity change $\delta C_i^m/C_0^m$ for each day $i = 1..21$ ($i = 0$ stands for the average over the 21 days) and each considered phase $m = 0, 1$

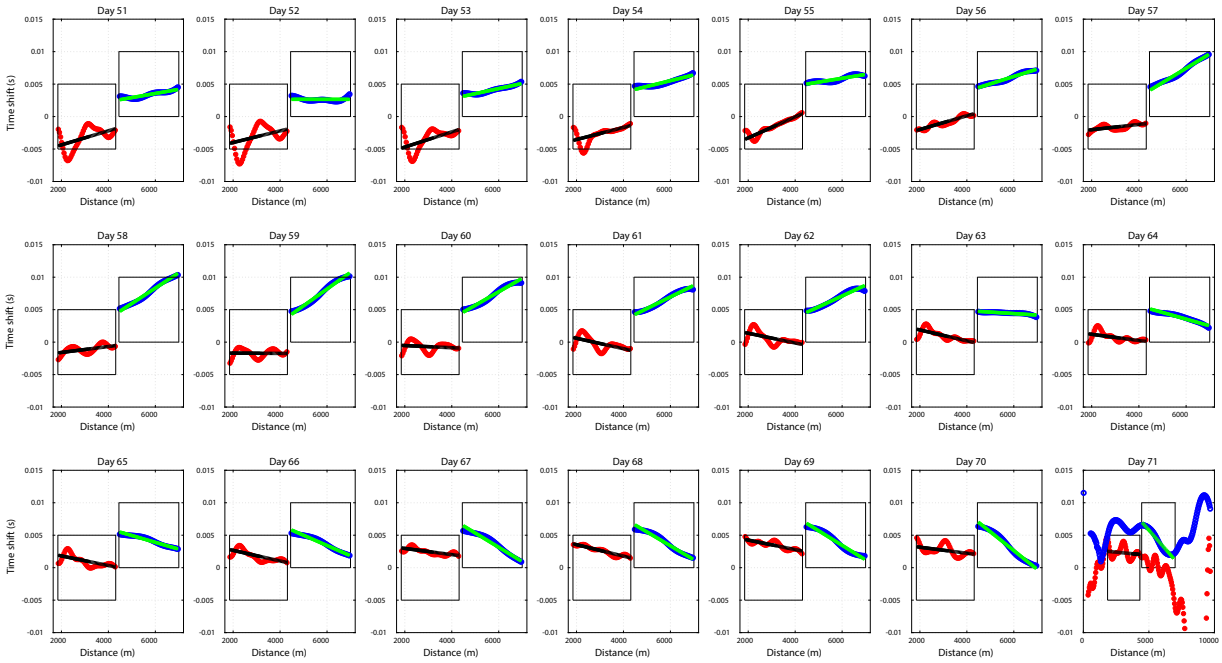

Figure 4. Daily time-shifts $\delta t^m(x)$ averaged over the frequencies for the fundamental mode (red dots) and the first overtone (blue dots) and the linear regressions used to estimate the relative phase velocity variations in black and green for the fundamental mode and the first overtone, respectively. The black boxes show the distance ranges over which the regression is performed. The results for the first overtone have been shifted vertically by 0.005 s to avoid clutter. For the day 71, we show the measurements along the whole offsets range.

(for the fundamental mode and the first overtone, respectively) following the approach of Brenguier et al. (2019). In this companion paper, Brenguier et al. (2019) showed that the relative velocity change can be computed as the (weighted) linear regression of the time-shifts δt along the offset x (Fig. 4) multiplied by the velocity of the considered phase:

$$\frac{\delta C_i^m}{C_0^m}(f) = -C_0^m(f)\frac{\Delta \delta t_i^m(f,x)}{\Delta x}\Bigg|_{x=x_{min}}^{x=x_{max}}, \tag{9}$$

where $\Delta Y/\Delta x$ stands for the linear regression of Y along x and x_{min} and x_{max} are the offset bounds between which the regression is performed. We will develop more in the Results section on how to chose these bounds. The standard errors of the linear regression gives the uncertainty of the relative velocity change.

3.3 Depth-dependent relative shear-wave velocity change

As shown by Haney & Tsai (2017) using a thin-layer finite-element method approach, the relative change in Rayleigh wave phase velocity $\mathbf{C}(f)$ for any given mode, at different frequencies (Fig. 5), due to a relative change in shear-wave velocity $\boldsymbol{\beta}(z)$ at depth is given by:

$$\frac{\delta \mathbf{C}}{\mathbf{C}}(f) = \mathbf{K}(f,z)\frac{\delta \boldsymbol{\beta}}{\boldsymbol{\beta}}(z)\,, \tag{10}$$

where $\mathbf{K}$ is a depth sensitivity kernel, f the frequency and z the depth. Equation 10 holds if one assumes that either (1) Poissons ratio and density are fixed or (2) P-wave velocity and density are fixed. In each case, the sensitivity kernel has to be adapted (see Haney & Tsai 2017, for details) and we modified Haney & Tsai (2017)'s code to output the corresponding $\mathbf{K}$ computed from an average velocity model of the area (Chmiel et al. 2019). In this work, we chose to fix the P-wave velocity and the density.

The relative shear-wave velocity perturbation can therefore be retrieved using a simple weighted-damped least squares inversion (Haney & Tsai 2017). Following Haney & Tsai (2017), we define the data covariance matrix as a diagonal matrix with the relative phase velocity uncertainties on the diagonal ($\mathbf{C_d} = \boldsymbol{\sigma}_d\mathbf{I}$) and the model covariance matrix as:

$$\mathbf{C_m}(i,j) = \sigma_m^2 \exp\left(-|z_i - z_j|/\lambda\right), \tag{11}$$

where $\sigma_m = \gamma\bar{\sigma_d}$ is the model standard deviation (γ is a user-defined tuning factor and $\bar{\sigma_d}$ is the average of the data uncertainties), z_i and z_j are the depths at the top of the ith and jth layers, and λ is a correlation length along depth. The parameters γ and λ are defined through a systematic grid-search of the data residual evolution with respect to γ and λ trial values, using a L-curve criterion (Hansen & OLeary 1993). The depth distribution of the shear-wave perturbations is obtained by solving the following system

$$\begin{bmatrix} \mathbf{C_d^{-1}K} \\ \mathbf{C_m^{-1}} \end{bmatrix} \frac{\delta \boldsymbol{\beta}}{\boldsymbol{\beta}} = \begin{bmatrix} \mathbf{C_d^{-1}} \\ \mathbf{0} \end{bmatrix} \frac{\delta \mathbf{C}}{\mathbf{C}}.$$

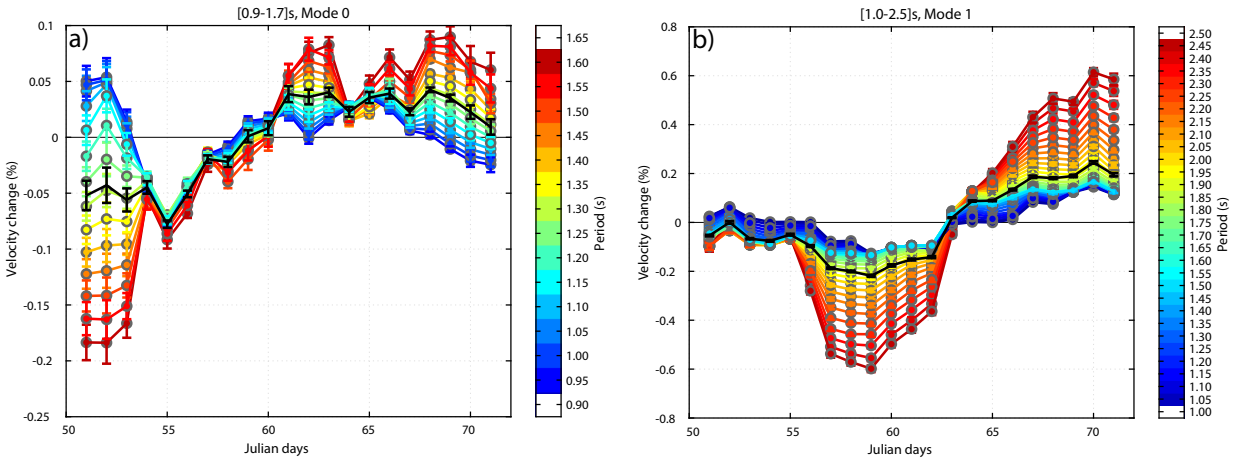

Figure 5. left) Daily, period-dependant relative phase velocity changes for the fundamental mode. right) Daily, period-dependant relative phase velocity changes for the first overtone. Note the difference in amplitude between the two modes. The black curves are obtained by averaging the time-shifts $\delta t_i^m(f,x)$ over the frequencies before performing the linear regression (shown in Fig.4).

4 RESULTS

The fundamental mode is analysed in the [0.6 - 1.1] Hz frequency band and the first overtone in the [0.4 - 1.0] Hz frequency band, where most of their energy is concentrated (Fig. 2b). The fundamental mode exhibit large amplitudes at frequencies lower than 0.5 Hz (Chmiel et al. 2019) but at these frequencies, the wavelengths become large compared to the size of the array which impedes the measurement of the time shift and reduces the distance range on which the linear regression can be performed. As shown in Figure 4, the time-shifts data do not exhibit a linear trend for the whole range of distances. At long distances, the $\delta t_i^m(x)$ measurements strongly oscillate (starting around 6.5-7 km) because of the lower signal to noise ratio of the stacked correlations which are much less numerous for these ranges. At short distance, we also observe rapid oscillations of the time-shifts for both fundamental mode and overtone. However, the fundamental mode measurements (red dots in Fig. 4) seems to stabilize at shorter distance ($\sim$2 km) than the overtone ($\sim$4.5 km). We hypothesize that this effect is a consequence of performing the time-shift measurements on waves in the near field where wave interference may occur. The dominant frequencies of 0.8 Hz and 0.6 Hz give wavelengths on the order of $\sim$600 m and $\sim$1400 m for the fundamental mode and the first overtone, respectively. The measurements are therefore stabilizing around three wavelengths for both phases, a distance at which the near-field effects become negligible. We chose to

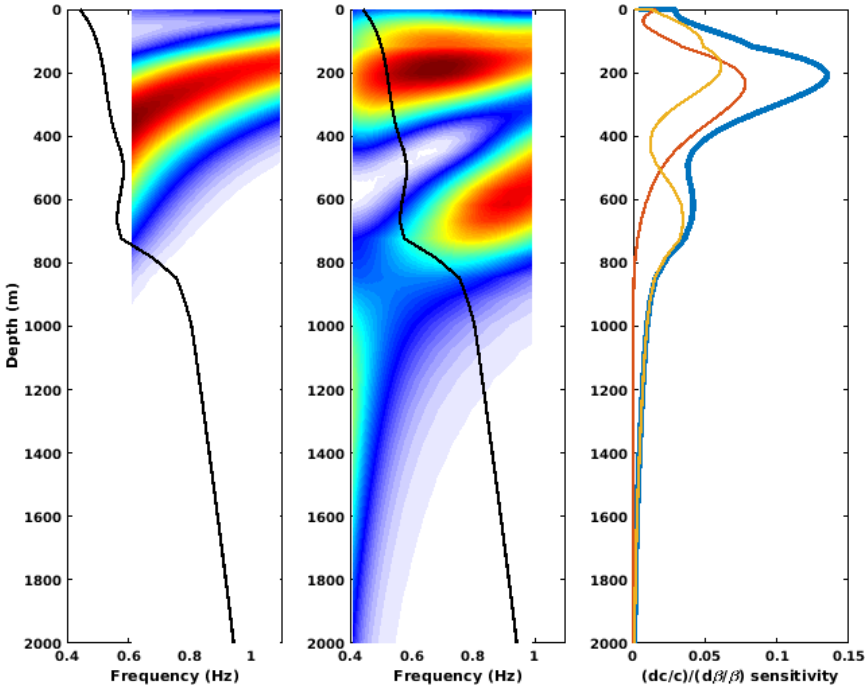

Figure 6. Depth sensitivity kernels for relative perturbations in shear-wave velocity with respect to relative perturbations in phase velocity for the fundamental mode (left) and the first overtone (middle). The right panel shows the frequency-averaged kernels (fundamental mode in red, first overtone in yellow) and their sum (in blue) showing the total extent of depth sensitivity when combing the two modes. The (normalized) shear-wave velocity model used for the computation is shown by the black curves.

perform the linear regressions along the distances corresponding to three to seven wavelengths. In the case of the overtone, seven wavelengths correspond to a distance larger than 7 km, we therefore restrict the maximum distance for this phase at 7 km. Extending the linear regression for the fundamental mode to 7 km would slightly change the estimated values of $\delta C_i^0/C^0$ but has little effect on the final estimation of the depth and amplitude of the shear-velocity changes.

Figure 5 shows the temporal variations of phase velocity for the two modes at different frequencies. Except for the three first days, the fundamental mode exhibit variations smaller than $\pm 0.1\%$ at all frequencies. In general, lower frequencies show larger velocity changes which suggests that the changes are happening deeper in the subsurface rather than shallower. This is confirmed by the shape of the depth sensitivity kernels for the fundamental mode (Fig. 6). In contrast, the overtone exhibits much larger temporal variations with amplitudes up to 0.6% at low frequency. For these frequencies lower than 0.5 Hz (above 2 s of period), the sensitivity of the overtone displays two maxima: a large amplitude one around 200 m depth and a lower amplitude one below 1000 m

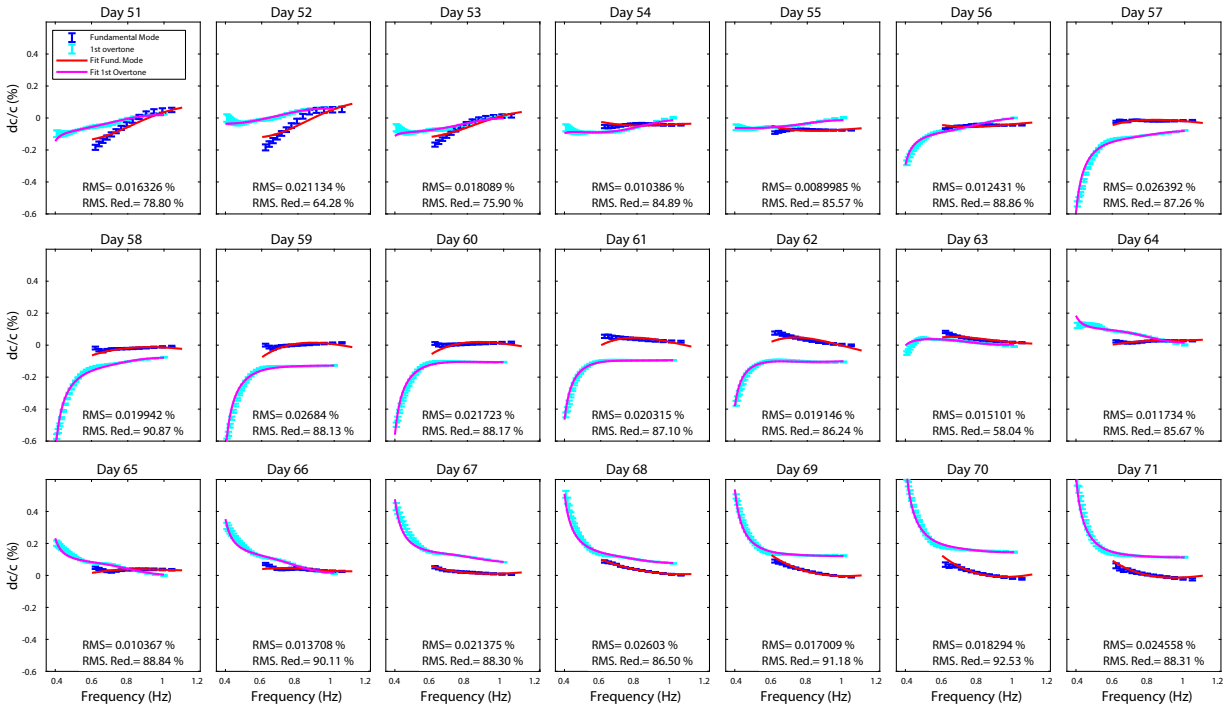

Figure 7. Daily differential phase velocity dispersion curves for the fundamental mode and the first overtone with their uncertainties (blue and cyan curves, respectively). The fit to the data after inversion is shown by the inverted dispersion curves in red and magenta for the fundamental mode and the first overtone, respectively. The daily misfit value as well as the misfit reduction from $\delta C/C = 0$ are shown at the bottom of each panel.

depth. The shallow sensitivity region overlaps with the sensitivity of the fundamental mode. The fact that the fundamental mode shows only small variations suggests that the large variations detected by the first overtone at low frequency are located deep in the subsurface.

These observations are confirmed by the joint inversion of the differential phase dispersion curves (Fig. 7). We used $\gamma = 12$ and $\lambda = 250m$ as smoothing and damping parameters. The fit to the data is good for every day meaning that we manage to find a model of relative shear-wave velocity change at depth that is consistent with both fundamental mode and first overtone daily observations. From Figure 7, we can see that the overtone data at low frequency explain most of the variance of the model. The final time-lapse results (Fig. 8) indeed show that the largest shear-wave variations (reaching $\pm$ 1.5%) are located below 800 m in the faster layer of the Chalk Group formation, while little or no variation is observed in the shallower North Sea Group sediments (Kruiver et al. 2017; Chmiel et al. 2019). The decrease of the amplitude below 1600 m is mostly

due to the vanishing of the sensitivity of the first overtone at these depths and we cannot rule out large velocity changes deeper in the subsurface.

5 DISCUSSION AND CONCLUSION

Ballistic wave travel-time from noise correlations are strongly sensitive to the noise sources distribution and its azimuthal variations during the monitoring period. The stacking procedure that we used is partly an azimuthal stacking and therefore helps to reduce the noise sources influence on the phase-shift measurements. Moreover, for the same dataset Brenguier et al. (2019) checked that the azimuthal variations of the noise could not induce travel-time uncertainties larger than 0.5%. The large velocity change that we observe below 1000 m cannot be explained by noise sources biases alone.

Observing large velocity variations in the Chalk layer and little variations in the Tertiary and Quaternary sediments is in good agreement with the observations made with ballistic P-wave on the same dataset (Brenguier et al. 2019). On one hand, the P-wave refracted at the top of the Chalk layer exhibits small variations during the first four days then its speed increases by $\sim$1% on days 55-56 before stagnating or slightly decreasing during the rest of the analysed period. On the other hand, the direct P-wave, which is sampling the first 200 m of the subsurface, shows a small decrease of velocity of about -0.25% during the first 12 days, then a 0.1% recovery. It has to be noted that the reference used in the P-wave study and the current work are different. Therefore, only the variations of velocity changes and their relative amplitudes can be compared. The refracted P-wave and the first overtone show same order of magnitude variations, consistent with their common sensitivity to the Chalk layer. Similarly, the fundamental mode and the direct P-wave, both sensitive to the shallower parts of the subsurface show little variations.

A clue about the nature of this deep velocity change can be found in the anti-correlation between the S-wave the P-wave velocity change. The only noticeable event that occurred during the monitoring period is a strong rainfall during days 51 to 54 with 40 mm of water (16 mm alone on day 54) following a 2 weeks period without rain. The increase of Vp coupled with the decrease of Vs would suggest a water saturation effect where water replaces air in pores (Fores et al. 2018).

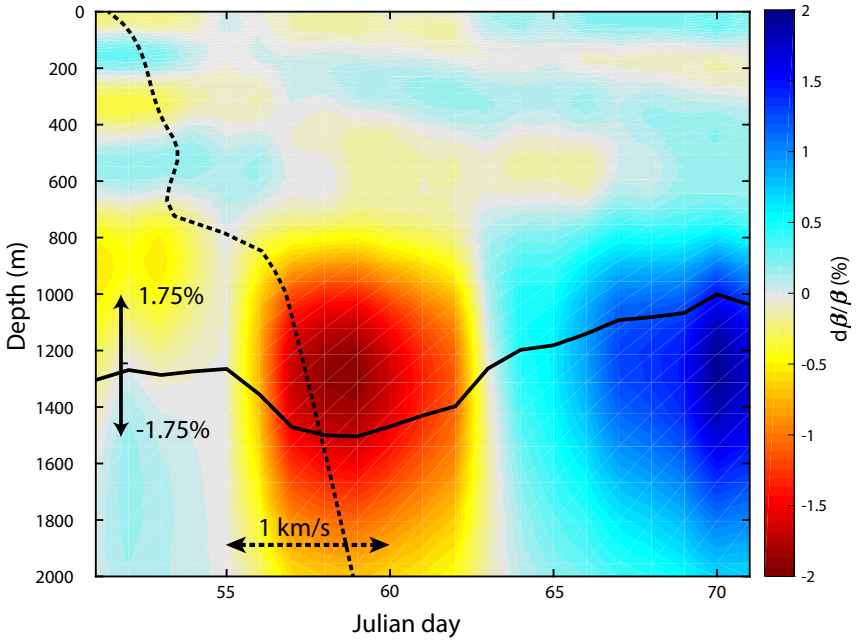

Figure 8. Depth-dependent relative shear-wave changes obtained by jointly inverting the frequency-dependent relative phase velocity variations of the fundamental mode and the first overtone. The average velocity change between 1000 m and 1500 m is shown by the plain black curve. Most of the changes happen in the Chalk layer below 1000 m depth. The average Vs model of the area is shown in dotted black curve for reference with the scale denoted by the dotted arrows.

The slow recovery after day 60 would come from the drainage of the Chalk layer. This fast effect could results from the high connectivity between the near surface and the Chalk produced by a dense network of fractures and faults (van Gent et al. 2010). To support the fluid substitution possibility, we used a poroelastic approach and particularly the Biot-Gassmann law generalized to the cases of a mixture of 2 fluids saturating the porous space (e.g., Dupuy et al. 2016), which allows us to quantify elastic velocity variations during fluid substitution processes. In the carbonate formations encountered at these depths, we considered a porous skeleton composed of calcite with a porosity of 20%, filled with a mixture of air and brine, the respective proportions of which vary. The consolidation parameter describing in particular the compressibility and shear properties of the porous skeleton was calibrated using seismic velocities estimated at this depth, in the order of 3300 m/s for Vp and 1300 m/s for Vs (this has little influence on the relative velocity variations as a function of saturation).

Figure 9a) shows that Vp can increase non-linearly from 2950 m/s (dry formation) to 3300 m/s

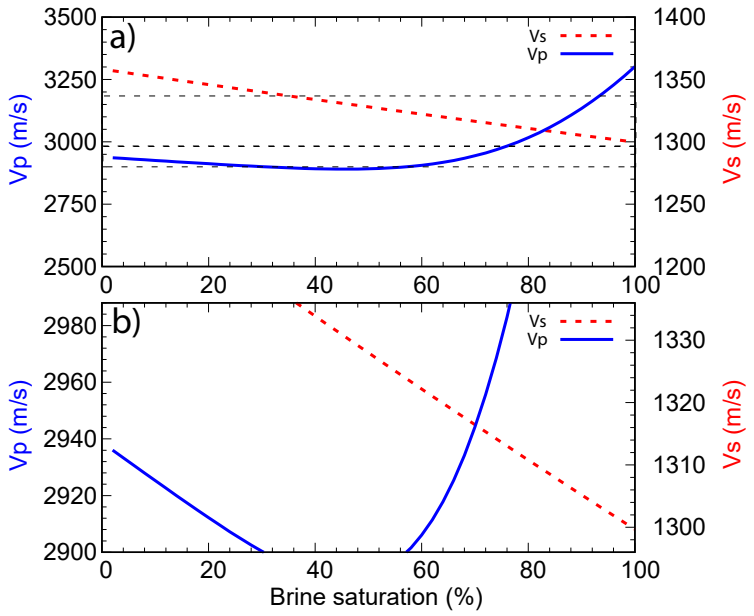

Figure 9. a) P- and S-wave velocity variations as a function of the saturation of the Chalk layer. b) Zoom in panel a) with the velocity axis centred around ±1.5% variations around the Vp and Vs values at 70% saturation.

(saturated material), while Vs decrease linearly from 1350 m/s (dry formation) to 1300 m/s (saturated material). It also shows that above 60% of saturations, a very small change in saturation can explain quantitatively the Vp and Vs variations observed from seismic noise analysis. It has to be noted that, although the variations in saturation can be locally large (several tens of percent at meters scale) the spatially broad sensitivity of the waves used in our analysis will only give homogenized and averaged values across hundreds meter scale (∼700-1300 m depth). Nevertheless, assuming that the Chalk layer saturation is at a value where the sensitivities of Vp and Vs to saturation changes are maximum (around 70% saturation), we can estimate that the saturation varied by about ±10% during the studied period as underlined in Figure 9b).

One of the main limitation of this new passive monitoring approach is the need for dense seismic arrays with a relatively large aperture to be able to perform a robust linear regression of the time-shifts along the offsets. Although such dense arrays are more and more common (e.g., Mordret et al. 2014b; Nakata et al. 2015; Ben-Zion et al. 2015), one would ideally like to perform the monitoring measurements on signals from a single pair of stations. One could therefore take advantage of sparse, but permanent or long-term seismic networks, the same way they are used for

CWI. It can be done because we can always measure the time-shift between 2 non-synchronous correlations from the same station pair using Equation 6. The relative (phase) velocity variation can then be estimated with

$$\frac{\delta v}{v_0} = -v_0 \frac{\delta t}{D} \,. \tag{12}$$

Here, v_0 is the phase velocity of the considered (ballistic) wave and D corresponds to the inter-station distance. However, without the averaging scheme presented in this paper, the ballistic waves can be strongly sensitive to variations in the seismic noise sources positions and properties which can mask the changes of interest in the subsurface.

We present in this study a novel approach to monitor the seismic velocity temporal changes using ambient noise correlations. Instead of measuring delays in the coda part of single pair of stations seismograms, we evaluate the time-shift of the ballistic Rayleigh waves, retrieved from a dense seismic network, as a function of the propagation distance to get the relative velocity changes. Using a wavelet-transform processing, we are able to extract frequency-dependent time-shifts for different modes. This enables us to invert the corresponding differential dispersion curves into 1D depth-dependent relative shear-wave velocity variation profiles. The information from two different Rayleigh wave modes helps to constrain the location of the changes at depth. The observed temporal velocity changes, reaching $\pm 1.5\%$, are likely hydrological in nature and the anti-correlation with P-wave velocity variations suggests a saturation variation effect. This method, generalized to any ballistic waves (Brenguier et al. 2019), paves the way to high temporal and spatial resolution monitoring studies and make passive time-lapse tomography of dynamic geological targets, such as volcano magma chambers, active tectonic faults or industrially exploited reservoirs, possible.

ACKNOWLEDGMENTS

AM acknowledges support from the National Science Foundation grant PLR-1643761. ISTerre is part of Labex OSUG@2020. This project received funding from the Shell Game Changer project

HiProbe. We acknowledge the European Research Council under grants no. 817803, FAULT-SCAN and no. 742335, F-IMAGE and the European Unions Horizon 2020 research and innovation program under grant agreement No 776622, PACIFIC. The data were provided by NAM (Nederlandse Aardolie Maatschappij). We acknowledge M. Campillo, N. Shapiro, G. Olivier, P. Roux, R. Brossier and C. Voisin for useful discussions. The authors thank Nederlandse Aardolie Maatschappij and Shell for permission to publish. The data are available upon request to NAM (W. Van der Veen).

REFERENCES

Ben-Zion, Y., Vernon, F. L., Ozakin, Y., Zigone, D., Ross, Z. E., Meng, H., White, M., Reyes, J., Hollis, D., & Barklage, M., 2015. Basic data features and results from a spatially dense seismic array on the San Jacinto fault zone, *Geophysical Journal International*, **202**(1), 370–380.

Boué, P., Poli, P., Campillo, M., Pedersen, H., Briand, X., & Roux, P., 2013. Teleseismic correlations of ambient seismic noise for deep global imaging of the Earth, *Geophysical Journal International*, **194**(2), 844–848.

Bourne, S., Oates, S., & van Elk, J., 2018. The exponential rise of induced seismicity with increasing stress levels in the Groningen gas field and its implications for controlling seismic risk, *Geophysical Journal International*, **213**(3), 1693–1700.

Brenguier, F., Campillo, M., Hadziioannou, C., Shapiro, N., Nadeau, R. M., & Larose, E., 2008a. Post-seismic relaxation along the San Andreas fault at Parkfield from continuous seismological observations, *science*, **321**(5895), 1478–1481.

Brenguier, F., Shapiro, N. M., Campillo, M., Ferrazzini, V., Duputel, Z., Coutant, O., & Nercessian, A., 2008b. Towards forecasting volcanic eruptions using seismic noise, *Nature Geoscience*, **1**(2), 126.

Brenguier, F., Campillo, M., Takeda, T., Aoki, Y., Shapiro, N., Briand, X., Emoto, K., & Miyake, H., 2014. Mapping pressurized volcanic fluids from induced crustal seismic velocity drops, *Science*, **345**(6192), 80–82.

Brenguier, F., Courbis, R., Mordret, A., Campman, X., Boué, P., Chmiel, M., Takano, T., Lecocq, T., Van der Veen, W., Postif, S., & Hollis, D., 2019. Noise-based Ballistic Body-wave Passive Seismic Monitoring, *submitted to Geophysical Journal International*.

Chmiel, M., Mordret, A., Boué, P., Brenguier, F., Lecocq, T., Courbis, R., Hollis, D., Campman, X., Romijn, R., & Van der Veen, W., 2019. Ambient noise multimode Rayleigh and Love wave tomography to determine the shear velocity structure above the Groningen gas field, *submitted to Geophysical Journal International*.

Clements, T. & Denolle, M. A., 2018. Tracking Groundwater Levels using the Ambient Seismic Field, *Geophysical Research Letters*, **45**(13), 6459–6465.

Colombi, A., Chaput, J., Brenguier, F., Hillers, G., Roux, P., & Campillo, M., 2014. On the temporal stability of the coda of ambient noise correlations, *Comptes Rendus Geoscience*, **346**(11), 307–316.

Corciulo, M., Roux, P., Campillo, M., & Dubucq, D., 2012. Instantaneous phase variation for seismic velocity monitoring from ambient noise at the exploration scale, *Geophysics*, **77**(4), Q37–Q44.

Donaldson, C., Caudron, C., Green, R. G., Thelen, W. A., & White, R. S., 2017. Relative seismic velocity variations correlate with deformation at Kīlauea volcano, *Science advances*, **3**(6), e1700219.

Dupuy, B., Garambois, S., & Virieux, J., 2016. Estimation of rock physics properties from seismic attributes – Part 1: Strategy and sensitivity analysis, *Geophysics*, **81**(3), M35–M53.

Durand, S., Montagner, J., Roux, P., Brenguier, F., Nadeau, R., & Ricard, Y., 2011. Passive monitoring of anisotropy change associated with the Parkfield 2004 earthquake, *Geophysical Research Letters*, **38**(13).

Fichtner, A., Kennett, B. L., Igel, H., & Bunge, H.-P., 2008. Theoretical background for continental-and global-scale full-waveform inversion in the time–frequency domain, *Geophysical Journal International*, **175**(2), 665–685.

Fores, B., Champollion, C., Mainsant, G., Albaric, J., & Fort, A., 2018. Monitoring Saturation Changes with Ambient Seismic Noise and Gravimetry in a Karst Environment, *Vadose Zone Journal*, **17**(1).

Froment, B., Campillo, M., Roux, P., Gouedard, P., Verdel, A., & Weaver, R. L., 2010. Estimation of the effect of nonisotropically distributed energy on the apparent arrival time in correlations, *Geophysics*, **75**(5), SA85–SA93.

Gassenmeier, M., Sens-Schönfelder, C., Delatre, M., & Korn, M., 2014. Monitoring of environmental influences on seismic velocity at the geological storage site for CO2 in Ketzin (Germany) with ambient seismic noise, *Geophysical Journal International*, **200**(1), 524–533.

Grinsted, A., Moore, J. C., & Jevrejeva, S., 2004. Application of the cross wavelet transform and wavelet coherence to geophysical time series, *Nonlinear processes in geophysics*, **11**(5/6), 561–566.

Haney, M. M. & Tsai, V. C., 2017. Perturbational and nonperturbational inversion of Rayleigh-wave velocities, *Geophysics*, **82**(3), F15–F28.

Hansen, P. C. & OLeary, D. P., 1993. The use of the L-curve in the regularization of discrete ill-posed problems, *SIAM Journal on Scientific Computing*, **14**(6), 1487–1503.

Kruiver, P. P., van Dedem, E., Romijn, R., de Lange, G., Korff, M., Stafleu, J., Gunnink, J. L., Rodriguez-Marek, A., Bommer, J. J., van Elk, J., et al., 2017. An integrated shear-wave velocity model for the Groningen gas field, The Netherlands, *Bulletin of Earthquake Engineering*, **15**(9), 3555–3580.

Kumar, P. & Foufoula-Georgiou, E., 1994. Wavelet analysis in geophysics: An introduction, *Wavelets in geophysics*, **4**, 1–43.

Labat, D., 2005. Recent advances in wavelet analyses: Part 1. A review of concepts, *Journal of Hydrology*, **314**(1-4), 275–288.

Larose, E., Carrière, S., Voisin, C., Bottelin, P., Baillet, L., Guéguen, P., Walter, F., Jongmans, D., Guillier, B., Garambois, S., et al., 2015. Environmental seismology: What can we learn on earth surface processes with ambient noise?, *Journal of Applied Geophysics*, **116**, 62–74.

Lecocq, T., Longuevergne, L., Pedersen, H. A., Brenguier, F., & Stammler, K., 2017. Monitoring ground water storage at mesoscale using seismic noise: 30 years of continuous observation and thermo-elastic and hydrological modeling, *Scientific Reports*, **7**(1), 14241.

Mainsant, G., Larose, E., Brönnimann, C., Jongmans, D., Michoud, C., & Jaboyedoff, M., 2012. Ambient seismic noise monitoring of a clay landslide: Toward failure prediction, *Journal of Geophysical Research: Earth Surface*, **117**(F1).

Mao, S., Campillo, M., van der Hilst, R. D., Brenguier, F., Stehly, L., & Hillers, G., 2018. High temporal resolution monitoring of small variations in crustal strain by dense seismic arrays, *Geophysical Research Letters*, **46**(1), 128–137.

Mao, S., Mordret, A., Campillo, M., Fang, H., & van der Hilst, R. D., 2019. A new wavelet-based approach for frequency-dependent ambient noise monitoring, *in prep.*.

Minato, S., Tsuji, T., Ohmi, S., & Matsuoka, T., 2012. Monitoring seismic velocity change caused by the 2011 Tohoku-oki earthquake using ambient noise records, *Geophysical Research Letters*, **39**(9).

Mordret, A., Jolly, A., Duputel, Z., & Fournier, N., 2010. Monitoring of phreatic eruptions using interferometry on retrieved cross-correlation function from ambient seismic noise: Results from Mt. Ruapehu, New Zealand, *Journal of Volcanology and Geothermal Research*, **191**(1-2), 46–59.

Mordret, A., Landès, M., Shapiro, N., Singh, S., & Roux, P., 2014a. Ambient noise surface wave tomography to determine the shallow shear velocity structure at Valhall: depth inversion with a Neighbourhood Algorithm, *Geophysical Journal International*, **198**(3), 1514–1525.

Mordret, A., Shapiro, N. M., & Singh, S., 2014b. Seismic noise-based time-lapse monitoring of the Valhall overburden, *Geophysical Research Letters*, **41**(14), 4945–4952.

Mordret, A., Mikesell, T. D., Harig, C., Lipovsky, B. P., & Prieto, G. A., 2016. Monitoring southwest Greenlands ice sheet melt with ambient seismic noise, *Science advances*, **2**(5), e1501538.

Mordret, A., Sun, H., Prieto, G. A., Toksöz, M. N., & Büyüköztürk, O., 2017. Continuous Monitoring of High-Rise Buildings Using Seismic Interferometry, *Bulletin of the Seismological Society of America*, **107**(6), 2759–2773.

Morlet, J., Arens, G., Fourgeau, E., & Giard, D., 1982a. Wave propagation and sampling theoryPart II: Sampling theory and complex waves, *Geophysics*, **47**(2), 222–236.

Morlet, J., Arens, G., Fourgeau, E., & Glard, D., 1982b. Wave propagation and sampling theoryPart I: Complex signal and scattering in multilayered media, *Geophysics*, **47**(2), 203–221.

Nakata, N. & Snieder, R., 2013. Monitoring a building using deconvolution interferometry. II: Ambient-vibration analysis, *Bulletin of the Seismological Society of America*, **104**(1), 204–213.

Nakata, N., Chang, J. P., Lawrence, J. F., & Boué, P., 2015. Body wave extraction and tomography at Long Beach, California, with ambient-noise interferometry, *Journal of Geophysical Research: Solid Earth*, **120**(2), 1159–1173.

Obermann, A., Planes, T., Larose, E., & Campillo, M., 2013. Imaging preeruptive and coeruptive structural and mechanical changes of a volcano with ambient seismic noise, *Journal of Geophysical Research: Solid Earth*, **118**(12), 6285–6294.

Pacheco, C. & Snieder, R., 2005. Time-lapse travel time change of multiply scattered acoustic waves, *The Journal of the Acoustical Society of America*, **118**(3), 1300–1310.

Planès, T., Mooney, M., Rittgers, J., Parekh, M., Behm, M., & Snieder, R., 2015. Time-lapse monitoring of

internal erosion in earthen dams and levees using ambient seismic noise, *Géotechnique*, **66**(4), 301–312.

Pyrak-Nolte, L. J. & Nolte, D. D., 1995. Wavelet analysis of velocity dispersion of elastic interface waves propagating along a fracture, *Geophysical Research Letters*, **22**(11), 1329–1332.

Ridder, S., Biondi, B., & Clapp, R., 2014. Time-lapse seismic noise correlation tomography at Valhall, *Geophysical Research Letters*, **41**(17), 6116–6122.

Rivet, D., Campillo, M., Shapiro, N. M., Cruz-Atienza, V., Radiguet, M., Cotte, N., & Kostoglodov, V., 2011. Seismic evidence of nonlinear crustal deformation during a large slow slip event in Mexico, *Geophysical Research Letters*, **38**(8).

Rivet, D., Brenguier, F., Clarke, D., Shapiro, N. M., & Peltier, A., 2014. Long-term dynamics of Piton de la Fournaise volcano from 13 years of seismic velocity change measurements and GPS observations, *Journal of Geophysical Research: Solid Earth*, **119**(10), 7654–7666.

Salvermoser, J., Hadziioannou, C., & Stähler, S. C., 2015. Structural monitoring of a highway bridge using passive noise recordings from street traffic, *The Journal of the Acoustical Society of America*, **138**(6), 3864–3872.

Sens-Schönfelder, C. & Wegler, U., 2006. Passive image interferometry and seasonal variations of seismic velocities at Merapi Volcano, Indonesia, *Geophysical research letters*, **33**(21).

Shapiro, N. M. & Campillo, M., 2004. Emergence of broadband Rayleigh waves from correlations of the ambient seismic noise, *Geophysical Research Letters*, **31**(7).

Snieder, R., Grêt, A., Douma, H., & Scales, J., 2002. Coda wave interferometry for estimating nonlinear behavior in seismic velocity, *Science*, **295**(5563), 2253–2255.

Teolis, A. & Benedetto, J. J., 1998. *Computational signal processing with wavelets*, vol. 182, Springer.

Toyokuni, G., Takenaka, H., Takagi, R., Kanao, M., Tsuboi, S., Tono, Y., Childs, D., & Zhao, D., 2018. Changes in Greenland ice bed conditions inferred from seismology, *Physics of the Earth and Planetary Interiors*, **277**, 81–98.

van Gent, H., Back, S., Urai, J. L., & Kukla, P., 2010. Small-scale faulting in the Upper Cretaceous of the Groningen block (The Netherlands): 3D seismic interpretation, fault plane analysis and regional paleostress, *Journal of Structural Geology*, **32**(4), 537–553.

van Thienen-Visser, K. & Breunese, J., 2015. Induced seismicity of the Groningen gas field: History and recent developments, *The Leading Edge*, **34**(6), 664–671.

Voisin, C., Garambois, S., Massey, C., & Brossier, R., 2016. Seismic noise monitoring of the water table in a deep-seated, slow-moving landslide, *SEG Interpretation*, **4**(3), SJ67–SJ76.

Voisin, C., Guzmán, M. A. R., Réfloch, A., Taruselli, M., & Garambois, S., 2017. Groundwater monitoring with passive seismic interferometry, *Journal of Water Resource and Protection*, **9**(12), 1414.

Wapenaar, K., Draganov, D., Snieder, R., Campman, X., & Verdel, A., 2010. Tutorial on seismic interferometry: Part 1Basic principles and applications, *Geophysics*, **75**(5), 75A195–75A209.

Weaver, R. L., Hadziioannou, C., Larose, E., & Campillo, M., 2011. On the precision of noise correlation interferometry, *Geophysical Journal International*, **185**(3), 1384–1392.

Wegler, U. & Sens-Schönfelder, C., 2007. Fault zone monitoring with passive image interferometry, *Geophysical Journal International*, **168**(3), 1029–1033.

Yukutake, Y., Ueno, T., & Miyaoka, K., 2016. Determination of temporal changes in seismic velocity caused by volcanic activity in and around Hakone volcano, central Japan, using ambient seismic noise records, *Progress in Earth and Planetary Science*, **3**(1), 29.